CrossMark
click for updates

3D-printing Ag-line of front-electrodes with optimized size and interface to enhance performance of Si solar cells†

Yi Jiang,[a] Yibo Chen,[a] Mingjian Zhang,[a] Yang Qiu,[a] Yuan Lin*[ab] and Feng Pan*[a]

The power conversion efficiency (PCE) of a Si solar cell strongly depends on the line width (LW) of the Ag front electrode lines and the quality of the Ag/Si interface (ASI). However, the correlation between these two aspects and the cell efficiency has not been systematically investigated before because of the difficulty to control the LW of the electrode line. In this work, a self-designed 3D-printing equipment was built. Based on it, we implement the printing of electrode lines with the controllable LW by systematically investigating various parameters, including the rheological characteristics of the silver paste and the printing parameters, such as nozzle inner diameter, pressure, stage speed and gap between nozzle and wafer. When applying electrode lines with different LWs on Si solar cells, a nearly linear relationship between the cell efficiency and the LW was found. Notably, a LW of 40 μm was achieved by using a nozzle with the inner diameter of 100 μm and controlling the printing parameters. When 3D-printed Ag front electrode lines with the LW of 40 μm were applied on Si solar cells, an about 1% efficiency improvement was implemented compared with the industrial Si solar cell. This efficiency improvement not only originated from the increasing radiation area by the narrower LW, but more importantly from the optimized ASI confirmed by the sectional TEM images. This study provides helpful guidance for future fabrication of front electrodes with optimized LW and ASI to improve the PCE of Si solar cells.

Introduction

Si solar cells play a key role in solving energy problems for current industrial applications due to the advantages of environment-friendly character and high power conversion efficiency (PCE).[1–4] One of the challenges for Si solar cells is the fabrication of front electrodes, which is important to the qualities of Si solar cells. Silver (Ag) paste has been widely used to fabricate front electrodes owing to its excellent electrical properties.[5] The traditional and industrial method for fabricating front electrodes is screen printing.[6–10] But there are several disadvantages for screen printing: (1) high fragmentation rate, due to direct contact between mask and wafer, greatly increases the cost of production; (2) large line-width (LW) leads to large optical loss with reduction effective light input; (3) nonuniform line height (LH) brings with conductivity loss. Generally, the LW, LH and aspect ratio (AR) (AR = LH/LW) of silver line prepared by screen printing are about 80 μm, 15 μm and 0.18,

respectively. This is almost the best level that screen printing technology could achieve, but could not fulfil the requirement of sustainable PCE improvement of Si solar cell. So it's necessary to find a new printing method to meet the needs of the industry. In recent years, many approaches had been adopted to make the silver electrodes, such as inkjet printing,[11–13] aerosol jet printing[14–16] and electrohydrodynamic (EHD) jet printing.[17,18] However, inkjet printing is limited by ink viscosity, aerosol jet printing is limited by nozzles and EHD jet printing is limited by the complex devices. They are all not suitable for the widely industrial applications.

3D printing technology is a kind of non-contact printing method, which has been used to fabricate front electrodes of solar cells. It has lower process cost with much more saving in material, and can greatly reduce the fragmentation rate due to the non-contact printing process. Lots of researchers have employed 3D printing to fabricate front electrodes of solar cells with small LW and high AR.[19,20] Kim *et al.* reported that 90 μm of LW and 0.2 of AR were achieved with a 50 μm diameter nozzle.[21] Chen *et al.* reported that 40 μm of LW and 0.85 of AR were achieved with a complex printing tool.[22] Beutel *et al.* reported that 35 μm of LW and 0.7 of AR were achieved with a special co-extrusion printing head.[23,24] Ahn *et al.* achieved electrode lines with 2 μm of LW and 0.7 of AR by a 1 μm diameter nozzle and special ink.[25] Based on these work, the efficiency of solar cell was found be greatly affected by the LW of electrode lines. Thus, correlation

[a]School of Advanced Materials, Peking University Shenzhen Graduate School, Shenzhen 518055, China. E-mail: panfeng@pkusz.edu.cn

[b]Institute of Chemistry, Chinese Academy of Sciences, Zhongguancun North First Street 2, 100190 Beijing, PR China. E-mail: linyuan@iccas.ac.cn

† Electronic supplementary information (ESI) available: Overview of the 3D printing equipment, the co-sintered temperature profile, SEM image. See DOI: 10.1039/c6ra08985b

between the LW of electrode lines and performance of Si solar cells will be necessary to be systematically investigated.

In this study, we developed a self-designed 3D printing equipment. Based on this device, the relationship between the LW of Ag electrode lines and various printing parameters, including nozzle inner diameter, pressure, the stage speed and the value of gap between the nozzle and wafer, was systematically investigated. Different LWs of electrode lines were fabricated by controlling these printing parameters. When applying them on Si solar cells with optimized ASI by controlling the co-sinter process, a nearly linear correlation between the cell efficiency and the LW was found. Comparing with the industrial solar cells, a 1% efficiency improvement was achieved when 3D-printed electrode lines with the LW of 40 μm were applied. Furthermore, related mechanism of efficiency improvement was also investigated.

Experimental

In this study, we assembled a self-designed 3D printing equipment to fabricate the front silver electrode of multicrystalline Si solar cells. Fig. S1† presents a brief overview of the 3D printing equipment. It consists of a 3D movable stage with control system, an air-powered dispenser and micro-nozzle.

A schematic diagram of the 3D printing process is illustrated in Fig. 1. The silver paste is loaded to a syringe and pushed by a positive pressure in a range of 0.1–0.6 MPa, which can be controlled by an air-powered dispenser (MUSASHI, ML-5000XII, Japan). The silver paste is squeezed out from a micro-nozzle (Fig. 1a, MUSASHI, FN-0.10ND-F, Japan) mounted at the bottom of the syringe, and directly transferred onto the wafer (Fig. 1b). In our 3D printer, a 3D movable stage with 1 μm precision (ZTGZ, ZT101EL200H, China) is fixed on a common baseplate. The syringe is fixed in Z-axis direction to adjust the gap between nozzle and wafer in a range of 40–120 μm, and keeps constant during the printing process. The wafer is placed on a holder which can move in X and Y direction with the speed of 5–30 mm s^{-1}. The printing processes are as follows: the silver

paste is squeezed out from the nozzle and deposited on the wafer when the XY stages are moving, and then forming the electrodes. So the main printing parameters include the inner diameter of nozzle, the positive pressure, the speed of movable stage and the gap between nozzle and wafer. As shown in Fig. 1c, the stereo structure of the silver paste is measured by a 3D confocal microscope, where the LW and LH of the electrode are 40 μm and 40 μm (AR is about 1), respectively. Fig. 1d presents the scanning electron microscopy (SEM) sectional image of the same electrode line.

The silver paste used in this work was supplied by an industry company. Its rheological property was studied by a steady and dynamic shear rheometer (RS600 model from Haak, with cone C35/1 sensor) at 25 °C.

In order to make the consistency of the experiments, we choose the semi-finished silicon wafer with SiN$_x$ layer and PN junction. The silicon wafer has the following properties: 39×52 mm^2 p-type wafers, cast poly-silicon with an as-cut thickness of 180 μm, and an emitter sheet resistance of 75 ± 2 Ω sq^{-1}. The front silver electrodes were fabricated on it by 3D printing.

After silver grid was printed on the wafer, the wafer was co-sintered in a seven zone belt furnace (KJ GROUP, Seven zone furnaces, China) with the temperature profile shown in Fig. S2.† The whole time of co-sinter was around 200 s.

Electrical and efficiency data of the solar cells were measured using a Sourcemeter (KEITHLEY, 2062A) under standard test conditions (25 °C, 100 mW cm^{-2}, AM1.5).

The morphology (LW and AR) of silver line was characterized by a 3D laser confocal microscope (Keyence, vk-x200, Japan).

Microstructural characterization of the Ag/Si interface was performed using scanning electron microscope (SEM, ZEISS Supra 55) and transmission electron microscope (TEM, FEI-TecnaiG2 30), respectively. The TEM sample was prepared by mechanical thinning and followed by focused-ion-beam (FIB) microsampling.

Results and discussion

1. The rheological characteristics of the silver paste

In order to control the morphology of the 3D printed electrode lines, we systematically studied the rheological properties of the silver paste firstly.

In a steady state rheological test, the viscosity curve was obtained by controlling the shear rate from 0.1 to 10 s^{-1}. The silver paste is highly viscous with a viscosity of 4×10^3 Pa s at a shear rate of 0.1 s^{-1}. However, the viscosity of the silver paste deceases very rapidly with the increasing shear rate. The viscosity become 538 Pa s at a shear rate of 2 s^{-1}, and smaller than 102 Pa s when the shear rate exceed 10 s^{-1}, as shown in Fig. 2a. The result of yield stress is produced by stress ramp technique, in which the shear stress is linearly increased at a constant rate from zero to a stress well above the yield stress. The values of shear elastic modulus (G') and viscous modulus (G'') are recorded over the shear stress from zero to 1000 Pa. As shown in Fig. 2b, both modulus decline obviously when the shear stress is larger than 300 Pa. Fig. 2c presents the dependence of the viscosity on time obtained by controlling the shear
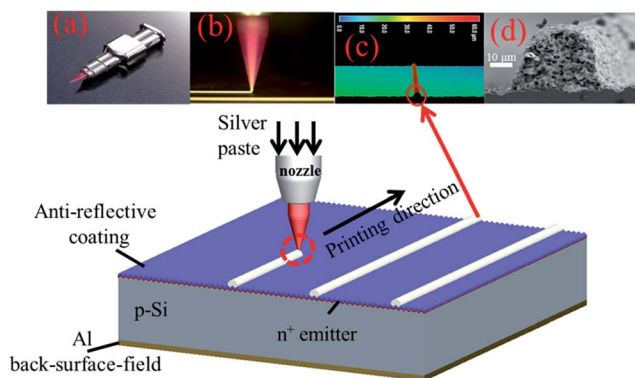
Fig. 1 Schematic diagram for the preparation process of electrode line by 3D printing. (a) The image of nozzle with diameter of 100 μm, (b) printing process recorded by a magnifying glass, (c) a 3D confocal microscope image of electrode line, (d) SEM sectional image of Ag front electrode.
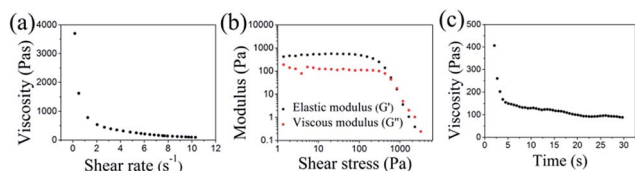
Fig. 2 (a) Silver paste viscosity as a function of shear rate, (b) shear elastic and viscous moduli as functions of applied shear stress, (c) silver paste viscosity as a function of time.

for 30 seconds at 10 s^{-1}. It is clear that the viscosity decreases with increasing time.

2. The effect of nozzle diameter on flow rate and flow velocity

In order to flexibly print electrode lines with different LWs by 3D printing, we systematically investigate the effects of the nozzle diameter on the morphology of the electrode lines. Three nozzles with different diameters (100 μm, 150 μm and 200 μm) were used, and the flow rate and flow velocity of silver filament were measured when adjusting the pressure. As shown in Fig. 3, it presents the flow rate and flow velocity as functions of the pressure from 0.2 to 0.45 MPa for three nozzles. Obviously, both the flow rate and flow velocity increase with the increasing pressure. The flow rate gets larger as the nozzle diameter increases, in consistent with our thought. Oppositely, the flow velocity decreases with increasing nozzle diameter. This fancy phenomenon could be explained by the balance between the shear stress and the osmotic pressure coexisted in the nozzle reported previously.[26–28] When the diameter of the nozzle increases, the average shear stress will decrease. Because the silver paste is a non-Newtonian fluid, its viscosity will increase with the decreasing of the shear stress, as presented in Fig. 2a. Accordingly, it is rational that the velocity decreases with the increasing nozzle diameter.

In order to obtain small LW of electrode line, low flow rate and high flow velocity are expected to obtain. Consequently, we chose the nozzle with diameter of 100 μm in the experiments below.

3. The effect of printing parameters on the LW of electrode line

Based on the results above, we chose a nozzle with the diameter of 100 μm to investigate the effects of other printing parameters,
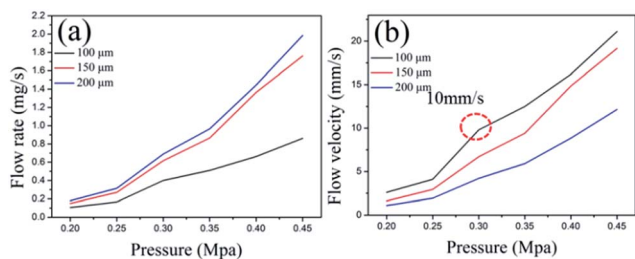
including pressure, the stage speed and the value of gap between the nozzle and wafer, on the morphology of electrode line. At first, we test the effect of pressure on the LW and AR. Fig. 4a and b show that the LW, LH and AR of electrode lines as functions of the pressure when the stage speed and the gap between nozzle and silicon wafer were fixed as 10 mm s^{-1} and 80 μm, respectively. The appropriate scope of pressure is 0.2–0.4 MPa here. There are two different phenomena, (1) the LW linearly increases with the increasing pressure; (2) the LH is basically constant with the increasing pressure. To explain the former one, the increasing pressure will lead to the increasing filamentary velocity (Fig. 3b), then it will pile up more silver paste on the silicon wafer. When the pressure exceeds 0.3 MPa, the filamentary velocity exceeds the stage speed, resulting in that the LW is increasingly bigger than nozzle diameter. While the pressure is lower than 0.3 MPa, the filamentary velocity is lower than stage speed. Then the part of the filament which has not contacted with the wafer will be stretched by the part of the filamentary that have been deposited on the wafer before, resulting in a smaller LW. But it seems that this stretching force is anisotropy, and the filament mainly undergoes stretching in the transverse direction and hardly in vertical direction. Thus the LH of silver electrode is almost the same (about 60 μm), as illustrated in Fig. 4a. So the LW becomes the only factor making AR decreases with the increasing pressure, as shown in Fig. 4b. It is clear that the electrode lines with the LW from 52 μm (about half of nozzle diameter 100 μm) to 175 μm (50% larger than nozzle diameter) were obtained here by adjusting the pressure.

To demonstrate the influence of stage speed on silver electrode, we fabricated a series of silver electrodes at different stage speeds. Their LW, LH and AR were plotted *vs.* the stage speed in Fig. 4c and d, when the pressure and the gap were fixed as 0.3 MPa and 80 μm, respectively. The LW decreases with increasing the stage speed, while the AR increases with increasing the stage speed. The relationship between the stage speed and the filamentary velocity is very important to the morphology of silver electrode. When the stage speed is slower than the filamentary velocity, it will lead to excessive filament deformation, otherwise it will result in filament discontinuities. As illustrated in Fig. 3b, the flow velocity of filament could be identified as 10 mm s^{-1} because the pressure, the gap and the nozzle diameter was fixed as 0.3 MPa, 80 μm and 100 μm, respectively in this test. When the stage speed gets to 10 mm s^{-1} in Fig. 4c, the LW is 98 μm which is nearly equal to the nozzle diameter (100 μm). In addition, the height has little change with increasing the stage speed, which has been explained above. This result further demonstrates that the filament mainly undergoes stretching in the transverse direction and hardly undergo in vertical direction. Usually when the pressure is 0.3 MPa, the appropriate range of the stage speed should be 6–20 mm s^{-1}, lower or higher stage speed will lead to the piled up of the filament or the discontinuities of electrode line. Finally, we obtained the electrode line with the LW of 70–120 μm by adjusting the stage speed.

According to the analysis above, we further investigated the effect of the gap on the LW when the pressure and the stage speed were chosen as 0.3 MPa and 10 mm s^{-1}. Fig. 4e and f

Fig. 3 (a) Flow rate as a function of pressure for nozzles with different diameters (100, 150 and 200 μm), (b) flow velocity as a function of pressure for nozzles with different diameters (100, 150 and 200 μm).
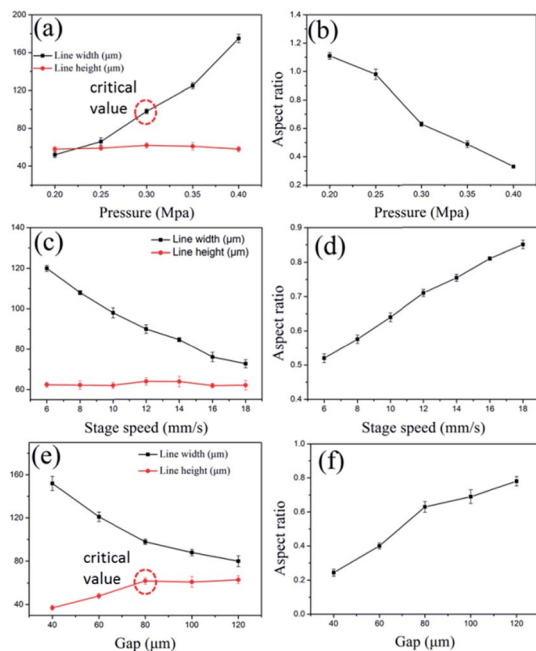
Fig. 4 The LW, LH and AR as functions of pressure (a and b), stage speed (c and d) and gap between nozzle and silicon wafer (e and f).

Fig. 5 The 3D laser confocal scanning microscope images of silver electrode lines with different LWs fabricated by 3D printing (a–d) and screen printing (e).

show the LW, the LH and the AR plot *vs.* the gap between nozzle and silicon wafer. As shown in Fig. 4e, when the gap is smaller than 80 μm, the LW is much larger than nozzle diameter (100 μm). Because the filament will be gashed by the nozzle and spread out on the wafer when the gap is too narrow. In addition, the LH also will be limited by the gap. The critical value of the gap is 80 μm for 0.3 MPa pressure. When the gap is greater than 80 μm, the morphology of filament is greatly related to the rheological or thixotropic characteristics of silver paste and the inner diameter of nozzle. The LW decreases, and LH keeps invariant with the increasing gap. Ockendon *et al.* demonstrated that silver filamentary length and radius is negatively correlated.[29] The radius of filament decreases with emerging length, which leads to narrower LW. This theory is consistent with our experiment. In the case of 0.3 MPa pressure and 10 mm s^{-1} stage speed, the appropriate value of the gap is 80–140 μm, otherwise the filament will be gashed or show discontinuities. In this part, the electrode lines with the LW of 80–152 μm were obtained by adjusting the gap between the nozzle and wafer.

In summary, the stage speed and the gap are negatively correlated with the LW, while the pressure is positively correlated with the LW. In addition, the height of the electrode is almost invariable when the silver paste and the diameter of nozzle are fixed.

4. The correlation between the efficiency of Si solar cells and the LW

Based on the study above, different LWs of electrode lines were prepared as the Ag front electrodes of Si solar cells. The electrodes displayed in Fig. 5a–d were fabricated by adjusting the pressure and the gap between nozzle and wafer, when the
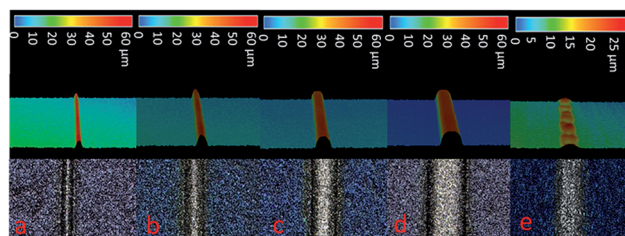
nozzle diameter and the stage speed were fixed as 100 μm and 10 mm s^{-1}, respectively. The corresponding printing parameters were listed in Table 1 in detail.

From Fig. 5a to d, the LW successively increases from 40 to 150 μm. In comparison, Fig. 5e shows the front electrode of industrial solar cell prepared by the traditional screen printing with the LW of 80 μm. Obviously, the front electrode by 3D printing is more uniform and controllable.

To compare the correlation between the efficiency of Si solar cells and the LW, we tested the *J–V* curves of the solar cells with different LWs and the industrial screen-printing solar cell. Fig. 6a, b and Table 2 display the *J–V* curves and related photovoltaic parameters of these five solar cells. Obviously, the efficiency of solar cell fabricated by 3D printing increases with the decreasing LW. The best efficiency of solar cell with the smallest LW is 17.51%, about 1% higher than the industrial screen-printing solar cell.

To discuss the mechanism of the efficiency (η) improvement, we calculated the relative improving percentage of each photovoltaic parameter such as V_{oc}, J_{sc}, and FF and exposure area with the decreasing LW listed in Table 2. For example, the V_{oc} and J_{sc} values of solar cells with LW of 75 μm are 605 mV and 38.22 mA cm^{-2}, respectively. When the LW decreases to 40 μm, the V_{oc} and J_{sc} values are 615 mV and 38.71 mA cm^{-2}, respectively. It could be derived that the relative improving quantities of V_{oc} and J_{sc} are 1.65% and 1.28%, respectively, when the exposure area increases by about 2%. Notably, only the increasing percent (about 5%) of FF could match with the relative improving percent (5%) of η. So we could conclude that the LW mainly affects the FF value, and then leads to the efficiency improvement. When the LW decreases from 75 to 40 μm, the area of the ASI decreases by about half. It means the recombination centers located at the ASI also decrease by about

Table 1 The printing parameters of electrodes with different LWs and ARs

LW (μm)	AR	Stage speed (mm s^{-1})	Pressure (MPa)	Gap (μm)
40	1.0	10	0.15	60
75	0.8	10	0.27	70
100	0.6	10	0.30	80
150	0.4	10	0.375	80
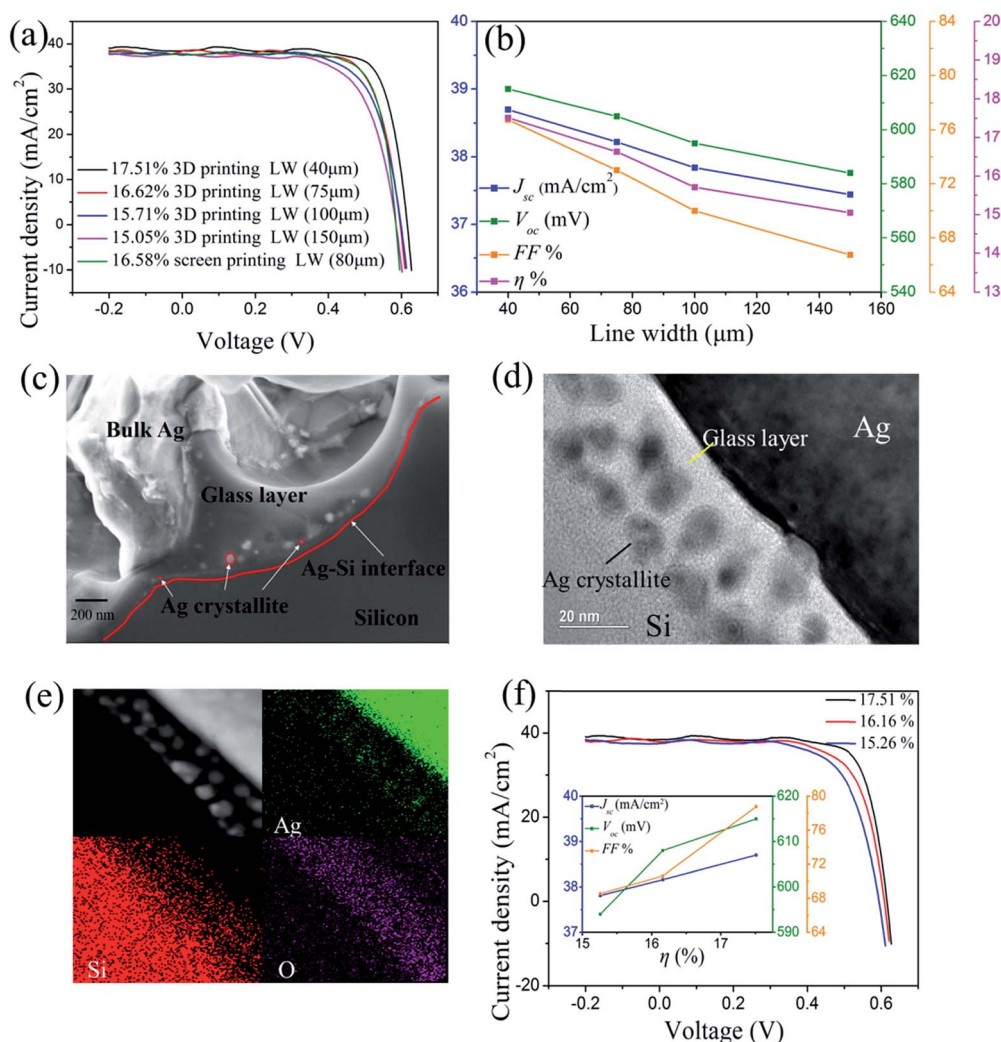
Fig. 6 (a) $J-V$ character curves of Si solar cells with different LWs of silver electrode lines, (b) the photovoltaic parameters as functions of the LWs, (c) the SEM image of Ag/Si interface of Si solar cell with LWs (40 μm) and PCE (17.51%), (d) the TEM image of the ASI with LWs (40 μm) and PCE (17.51%), (e) the EDS image of the ASI with LWs (40 μm) and PCE (17.51%), (f) $J-V$ character curves of the Si solar cells with the same LW under different heating processes (the inset compares the photovoltaic parameters of these Si solar cells).

half, which brings with the significant increase of FF. Beside the area effect of the ASI, the quality of ASI is also important for PCE. As shown in Fig. 6c, it presented the SEM image of the ASI in the solar cell with the best efficiency (17.51%), a continuous Ag line (along the red line) composed with small Ag crystallites were clearly observed at the ASI. The TEM and EDS data also verified the existence of Ag crystallites on ASI, as shown in

Fig. 6d and e. Ag crystallite on Si could serve as current pickup points and that conduction from the Ag crystallite to Ag bulk takes place *via* tunneling through the ultrathin glass layer in between.[30] In addition, we compared the Si solar cells with the same LW under different heating processes, as shown in Fig. 6d. Fig. S3† presented the SEM image of the Si solar cells with lower efficiency (15.26%) which has a discontinuous Ag crystallite line compared to the better Si solar cells. So we could conclude that the efficiency of solar cells can be enhanced by optimizing the LW and ASI of front electrodes.

Conclusions

In this study, we systematically investigated the rheological characteristics of the silver paste and the influence of printing parameters (pressure, stage speed and gap) on the morphology of Ag front electrode line based on a 3D printer assembled by our group. The linear relationship between the LW of electrode

Table 2 The photovoltaic parameters of Si solar cells with different line widths

LW (μm)	Exposure area (%)	V_{oc} (mV)	J_{sc} (mA cm^{-2})	FF (%)	η (%)
40	97.6	615	38.71	76.75	17.51
75	95.6	605	38.22	73.01	16.62
100	94.2	595	37.84	70.00	15.71
150	91.4	584	37.44	66.73	15.05
80 (screen)	95.3	585	37.60	75.62	16.58

line and these printing parameters was established, and the electrode lines with various LWs could be controllably fabricated by adjusting these printing parameters. When applying these Ag front electrode lines on Si solar cells, the efficiency of Si solar cell was linearly increasing with the decreasing of LW of the electrode line. Remarkably, a best efficiency of 17.51% was obtained when the LW was 40 μm, 1% higher than that of the industrial cell. In addition, the ASI quality could be optimized by controlling the co-sinter process. This study demonstrates the potential application of 3D printing method on the Si solar cell, and further illuminates the great potential on improving the efficiency of solar cell by searching the optimal printing parameters and the co-sinter processes.

Acknowledgements

Notes and references

1 B. O'Regan and M. Gratzel, *Nature*, 1991, **353**, 737–740.
2 H. Hoppe and N. S. Sariciftci, *J. Mater. Res.*, 2011, **19**, 1924–1945.
3 W. U. Huynh, J. J. Dittmer and A. P. Alivisatos, *Science*, 2002, **295**, 2425–2427.
4 M. C. Scharber, D. Mühlbacher, M. Koppe, P. Denk, C. Waldauf, A. J. Heeger and C. J. Brabec, *Adv. Mater.*, 2006, **18**, 789–794.
5 G. Guo, W. Gan, F. Xiang, J. Zhang, H. Zhou, H. Liu and J. Luo, *J. Mater. Sci.: Mater. Electron.*, 2010, **22**, 527–530.
6 W. J. Hyun, S. Lim, B. Y. Ahn, J. A. Lewis, C. D. Frisbie and L. F. Francis, *ACS Appl. Mater. Interfaces*, 2015, **7**, 12619–12624.
7 F. C. Krebs, M. Jørgensen, K. Norrman, O. Hagemann, J. Alstrup, T. D. Nielsen, J. Fyenbo, K. Larsen and J. Kristensen, *Sol. Energy Mater. Sol. Cells*, 2009, **93**, 422–441.
8 F. C. Krebs, *Sol. Energy Mater. Sol. Cells*, 2009, **93**, 465–475.
9 D. Schwanke, J. Pohlner, A. Wonisch, T. Kraft and J. Geng, *J. Microelectron. Electron. Packag.*, 2009, **6**, 13–19.
10 S. Ito, P. Chen, P. Comte, M. K. Nazeeruddin, P. Liska, P. Péchy and M. Grätzel, *Prog. Photovoltaics*, 2007, **15**, 603–612.
11 S. Mun, S. Yun, H. Jung and J. Kim, *Curr. Appl. Phys.*, 2012, **12**, e10–e13.
12 D.-Y. Shin, *J. Micromech. Microeng.*, 2010, **20**, 125003.
13 E. A. Roth, T. Xu, M. Das, C. Gregory, J. J. Hickman and T. Boland, *Biomaterials*, 2004, **25**, 3707–3715.
14 A. Mette, P. L. Richter, M. Hörteis and S. W. Glunz, *Prog. Photovoltaics*, 2007, **15**, 621–627.
15 C. Yang, E. Zhou, S. Miyanishi, K. Hashimoto and K. Tajima, *ACS Appl. Mater. Interfaces*, 2011, **3**, 4053–4058.
16 A. Mahajan, C. D. Frisbie and L. F. Francis, *ACS Appl. Mater. Interfaces*, 2013, **5**, 4856–4864.
17 D.-Y. Shin, J.-Y. Seo, H. Tak and D. Byun, *Sol. Energy Mater. Sol. Cells*, 2015, **136**, 148–156.
18 Y. Jang, I. Hartarto Tambunan, H. Tak, V. Dat Nguyen, T. Kang and D. Byun, *Appl. Phys. Lett.*, 2013, **102**, 123901.
19 J. A. Lewis, *Adv. Funct. Mater.*, 2006, **16**, 2193–2204.
20 C. Ladd, J. H. So, J. Muth and M. D. Dickey, *Adv. Mater.*, 2013, **25**, 5081–5085.
21 D.-H. Kim, S.-S. Ryu, D. Shin, J.-H. Shin, J.-J. Jeong, H.-J. Kim and H. S. Chang, *Mater. Sci. Eng., B*, 2012, **177**, 217–222.
22 X. Chen, K. Church, H. Yang, I. B. Cooper and A. Rohatgi, *IEEE*, 2011, 003667–003671.
23 M. Beutel, A. Lewis, M. Prondzinski, F. Selbmann, P. Richter, F. Bamberg, P. Raschtschepkin, A. Krause, C. Koch, M. Hentsche, K. H. Stegemann, E. Schneiderlöchner and H. Neuhaus, *Sol. Energy Mater. Sol. Cells*, 2014, **131**, 64–71.
24 L. P. Richter, G. Fischer, L. Sylla, M. Hentsche, S. Steckemetz, M. Müller, C. L. Cobb, S. E. Solberg, R. Rao, S. Elrod, P. Palinginis, E. Schneiderlöchner and D. H. Neuhaus, *Sol. Energy Mater. Sol. Cells*, 2015, **142**, 18–23.
25 B. Y. Ahn, E. B. Duoss, M. J. Motala, X. Guo and S.-I. Park, *Science*, 2009, **323**, 1590–1593.
26 J. Bruneaux, D. Therriault and M.-C. Heuzey, *J. Micromech. Microeng.*, 2008, **18**, 115020.
27 A. Delime and M. Moan, *Rheol. Acta*, 1991, **30**, 131–139.
28 H. A. Barnes, *J. Non-Newtonian Fluid Mech.*, 1995, **56**, 221–251.
29 H. Ockendon, *European Journal of Mechanics, B: Fluids*, 2001, **20**, 157–158.
30 C.-H. Lin, S.-Y. Tsai, S.-P. Hsu and M.-H. Hsieh, *Sol. Energy Mater. Sol. Cells*, 2008, **92**, 1011–1015.